instability in the resistance, which we have associated with excitation of the thin-layer moment relative to the thick-layer moment, does have an approximately linear dependence versus H for H greater than the saturation field, although on a fine scale, there are deviations not observed in previous studies (Fig. 3) (7, 9). Subsequent transitions at higher bias, which we have associated with magnetic excitations within the Co layers, show more complicated behavior. The measured zero-field intercepts of I_{crit} for the first transition are generally a factor of 2 to 4 lower than those derived from Eq. 2. We consider this satisfactory agreement, since the layers undoubtedly have nonuniform thickness. The observed slopes of I_{crit} versus H also agree with Eq. 2, provided that we assume a value for the phenomenological damping parameter $\alpha_G = 0.05$ to 0.2, which is unusually large compared to more macroscopic samples (5). However, we are in a new regime, and there may be large contributions to damping near normal/ferromagnetic interfaces (3) and from intralayer processes for nanometer-scale domains.

Our results have both good and bad implications for applications. The bad news is that the existence of magnetic switching caused by spin transfer places a limit on the current (and therefore the signal levels) that can be used for measuring GMR devices. The good news is that the spin-switching effect may enable magnetic random-access memories in which the memory elements are controlled by local exchange-effect forces rather than by long-range magnetic fields. Slonczewski predicts that the spin-transfer torques should dominate over the effects of the self-magnetic fields from flowing currents for devices up to about 100 nm in diameter (2), so that the point-contact geometry, with its intrinsically low GMR values, should not be necessary to employ the effect.

References and Notes
1. For reviews of the science and applications of GMR materials, see the collection of articles in *IBM J. Res. Dev.* **42**, (January 1998). (available electronically at www.research.ibm.com/journal/rd42-1.html)
2. J. Slonczewski, *J. Magn. Magn. Mater.* **159**, L1 (1996).
3. L. Berger, *Phys. Rev. B* **54**, 9353 (1996).
4. Ya. B. Bazaliy, B. A. Jones, S.-C. Zhang, *ibid.* **57**, R3213 (1998).
5. J. Slonczewski, *J. Magn. Magn. Mater.* **195**, L261 (1999).
6. R. N. Louie, thesis, Cornell University, Ithaca, NY (1997).
7. M. Tsoi *et al.*, *Phys. Rev. Lett.* **80**, 4281 (1998); erratum, *ibid.* **81**, 493 (1998).
8. J.-E. Wegrowe *et al.*, *Europhys. Lett.* **45**, 626 (1999).
9. J. Z. Sun, *J. Magn. Magn. Mater.* **202**, 157 (1999).
10. K. S. Ralls, R. A. Buhrman, R. C. Tiberio, *Appl. Phys. Lett.* **55**, 2459 (1989).
11. A. G. M. Jansen, A. P. van Gelder, P. Wyder, *J. Phys. C* **13**, 6073 (1980).
12. Fig. 2, B through E, exhibits samples never exposed to a magnetic field, but there are no qualitative differences as a function of magnetic history, as long as $H = 0$.
13. For a review, see M. A. M. Gijs and G. E. W. Bauer, *Adv. Phys.* **46**, 285 (1997).
14. Point-contact measurements of Cu/Co multilayers have previously shown small GMR values; see (6) and M. V. Tsoi, A. G. M. Jansen, J. Bass, *J. Appl. Phys.* **81**, 5530 (1997).
15. We thank J. Slonczewski, S. Guéron, and R. H. Silsbee for discussions. The work was supported by the NSF Materials Research Science and Engineering Centers program (DMR-9632275), the Sloan and Packard Foundations, the Office of Naval Research (N00014-97-1-0745), and Defense Advanced Research Projects Agency, and was performed in part at the Cornell node of the National Nanofabrication Users Network, supported by the NSF. E.B.M. was supported by a U.S. Department of Education grant.

Galileo Imaging of Atmospheric Emissions from Io

P. E. Geissler,[1]* A. S. McEwen,[1] W. Ip,[2] M. J. S. Belton,[3] T. V. Johnson,[4] W. H. Smyth,[5] A. P. Ingersoll[6]

The Galileo spacecraft has detected diffuse optical emissions from Io in high-resolution images acquired while the satellite was eclipsed by Jupiter. Three distinct components make up Io's visible emissions. Bright blue glows of more than 300 kilorayleighs emanate from volcanic plumes, probably due to electron impact on molecular sulfur dioxide. Weaker red emissions, possibly due to atomic oxygen, are seen along the limbs, brighter on the pole closest to the plasma torus. A faint green glow appears concentrated on the night side of Io, possibly produced by atomic sodium. Io's disk-averaged emission diminishes with time after entering eclipse, whereas the localized blue glows brighten instead.

Previous spacecraft and ground-based observations have yielded several indications of a tenuous atmosphere on Io. Dominated by SO_2 and its dissociation products SO, O, and S, Io's atmosphere has been studied at wavelengths ranging from the microwave to the ultraviolet (UV) (1, 2). Atomic O, S, Na, and K have been detected in extended neutral clouds escaping from the satellite (3), and recent Hubble Space Telescope (HST) observations of Io have imaged intense auroral emissions at far-UV wavelengths (4). Visible emissions from Io during eclipse by Jupiter were seen by Voyager 1 (5) and suggested to be due to molecular SO_2 (6). HST (7) and ground-based (8, 9) eclipse observations have detected neutral O and Na emissions from Io at visible wavelengths.

The Galileo spacecraft, in orbit around Jupiter since December 1995, can observe optical emissions from Io at a higher spatial resolution than previously possible and from a variety of perspectives unattainable from Earth (10). Diffuse emissions from Io have been seen in 16 distinct solid state imager (SSI) observations acquired during 14 eclipses over the course of

10 orbits. Recorded partly to monitor thermal emission from discrete volcanic centers (11), these observations provide a detailed look at visible aurorae on a solar system satellite. The bulk of the data was acquired with the SSI clear filter, which covers wavelengths between 380 and 1040 nm (12). Two sequences included visible color imaging using the SSI violet (380 to 445 nm), green (510 to 605 nm), and red (615 to 710 nm) filters. Diffuse emissions from Io have not been detected in any of the longer wavelength infrared SSI filters. Here, we describe the morphology of the optical emissions from Io, estimate their brightnesses and radiated powers, and suggest possible interpretations.

The most complete set of eclipse images was acquired on 31 May 1998 during the first of two eclipses in orbit E15 (13) (Table 1). These pictures were centered near a longitude of 70°W, on the orbital leading hemisphere of Io that is also the location of the plasma wake. One set of color images in the violet, green, red, and 1-μm (935 to 1090 nm) filters was taken along with two clear-filter pictures comparing Io's appearance 11 min after the start of the eclipse with its appearance 42 min later. The clear-filter images showed diffuse atmospheric emissions as well as discrete volcanic hot spots on Io's leading hemisphere, whereas only the hot spots were visible in the 1-μm filter. Diffuse emissions with three distinct distributions were seen in the visible color frames (Figs. 1 and 2A). The brightest emissions were blue glows close to the equator near the sub- and anti-Jupiter points, extending several hundred kilometers above the limb. They were seen at red, green, and violet wavelengths but were

[1]Lunar and Planetary Laboratory, University of Arizona, Tucson, AZ 85711, USA. [2]Institute of Astronomy, National Central University, Chung-Li, Taiwan 320, Republic of China. [3]National Optical Astronomy Observatories, Tucson, AZ 85719, USA. [4]Jet Propulsion Laboratory, MS 23-201B, 4800 Oak Grove Drive, Pasadena, CA 91109, USA. [5]Atmospheric and Environmental Research, 840 Memorial Drive, Cambridge, MA 02139, USA. [6]Division of Geology and Planetary Sciences, California Institute of Technology, Pasadena, CA 91125, USA.

*To whom correspondence should be addressed. E-mail: geissler@lpl.arizona.edu

brightest in the violet bandpass. A second, weaker glow running continuously along the limb was seen primarily in the red-filter image and was particularly bright along the north polar limb. The third component was a faint glow against the disk of Io at green-filter wavelengths. In the E15 observations, this green glow was concentrated on the night side of Io. Qualitatively similar emission distributions were seen in the noisier color eclipse data from orbit G7, except that the red polar limb glow was brighter in the southern hemisphere than in the northern hemisphere.

In calibrated images (14), the brightness of the equatorial blue glows reached >300 kilorayleighs (kR), easily visible to the naked eye (Table 2). This is consistent with the Voyager 1 measurement, which showed glows of several digital numbers above background and had a detection limit of 30 kR (5). We estimate that the total optical power (15) from Io was ~2 × 10^9 W. The blue glows in the E15 clear-filter observations contributed 1.5 × 10^8 W, with ~60% coming from the anti-Jupiter side. The optical power from the red polar limb glow amounted to 1 × 10^8 W, whereas the larger night-side disk glow accounted for ~7 × 10^8 W, with 1.6 × 10^8 W in the green filter alone. For comparison, ~3 × 10^8 W are expended in visible emissions from each of Io's flux-tube footprints on Jupiter (16).

Time variability of the emissions is suggested by differences between the two clear-filter images from the first eclipse of orbit E15. Io dimmed noticeably as time elapsed after the start of the eclipse (Fig. 2C). Io's disk-integrated brightness was ~30% greater in the observation taken 11 min after entry into Jupiter's shadow than it was in the later observation taken 53 min after eclipse entry. Some of this darkening might be due to a decrease in the amount of light scattered by Jupiter's atmosphere as the satellite moved deeper into the planet's shadow, but the dimming is apparent even on the side of Io facing away from Jupiter. More surprisingly, the localized equatorial plume glows appeared to brighten by 37% over the same time interval. A similar reduction in Io's total radiance with elapsed time in Jupiter's shadow was seen during the second eclipse of orbit E15, but quantitative measurements cannot be derived from the noisy and badly smeared images. Dimming of UV emissions from atomic O and S in Io's atmosphere upon ingress into Jupiter's shadow has also been observed by HST (17).

To investigate how the emission morphology varies with jovian magnetic longitude, we compared the E15 clear-filter images to previous clear-filter observations (18). Jupiter's magnetic field is tilted with respect to the planet's rotation axis, so the equator of the jovian magnetic field and the center of Io's plasma torus oscillate above and below Io's orbital plane (19). We compared one of the E15 images to two earlier clear-filter eclipse images acquired with similar viewing geometries on orbits G7 and G8 (Fig. 2B) and found that the pole with the brightest limb emission alternated between the north and south. The G7 and G8 observations were made while Io was at System III magnetic longitudes of 165° and 261°, respectively. At these locations, the center of the plasma torus was to the south of Io, on the same side as the brighter polar limb glows. Similarly, the limb glow during E15 (magnetic longitude of 72°) is brighter in the north, the same side of Io as the plasma torus position. This correspondence between polar limb glow brightness and the location of the torus center appears to be true of the other available clear-filter eclipse images as well [see supplementary table (available at www. sciencemag.org/feature/data/1039991.shl)]. In each case, the limb glow was brightest on the pole that was closest to the equator of the jovian magnetic field at the time of the observation. Io's polar UV emissions (4) and optical O emission (7) have been noted to display similar behavior.

During orbits G7, G8, and E15, the brightest glows on the sub- and anti-Jupiter hemispheres were associated with fixed geographic locations

Table 1. Galileo SSI Io eclipse observations during the first of two eclipses in orbit 15. Image times are spacecraft event times, uncorrected for light travel time to Earth. The eclipse began at 1998:151:00:06:17.482 GMT (year:day:hours:minutes:seconds). The effective spatial resolution (Res.) is lower than the data listed, because the images are smeared over several pixels because of the long exposure times. λ_{III} refers to Io's position with respect to Jupiter's magnetic field. Lat., latitude; Long., longitude; deg., degrees.

Obser-vation	Image number	Picture number	Filter	Lat. (deg.)	Long. (deg.)	Res. (km/pixel)	Image time (GMT)	λ_{III} long. (deg.)
CLR1	449843800	15I0004	Clear	−0.33	68.23	13.97	1998:151:00:17:07.511	53
GRN	449847102	15I0006	Green	−0.34	71.43	13.53	1998:151:00:50:41.389	68
RED	449847302	15I0007	Red	−0.34	71.63	13.50	1998:151:00:52:42.722	69
VIO	449847502	15I0008	Violet	−0.34	71.82	13.48	1998:151:00:54:44.056	70
CLR2	449847913	15I0022	Clear	−0.34	72.20	13.42	1998:151:00:58:43.510	72

Fig. 1. Enhanced visible color (red, green, and violet) image of Io in eclipse (left) compared to a sunlit view of Io from a similar perspective (right). Three distinct components make up Io's visible aurorae. Bright blue glows emanate from volcanic plumes near the sub- and anti-Jupiter points (longitudes of 0° and 180°). Weaker red glows are seen along the polar limbs, brighter in the north than in the south. A faint green glow appears against the disk of Io, concentrated on the night side (longitudes of 90° and beyond). The red and green glows appear brighter than natural in this contrast-stretched picture.
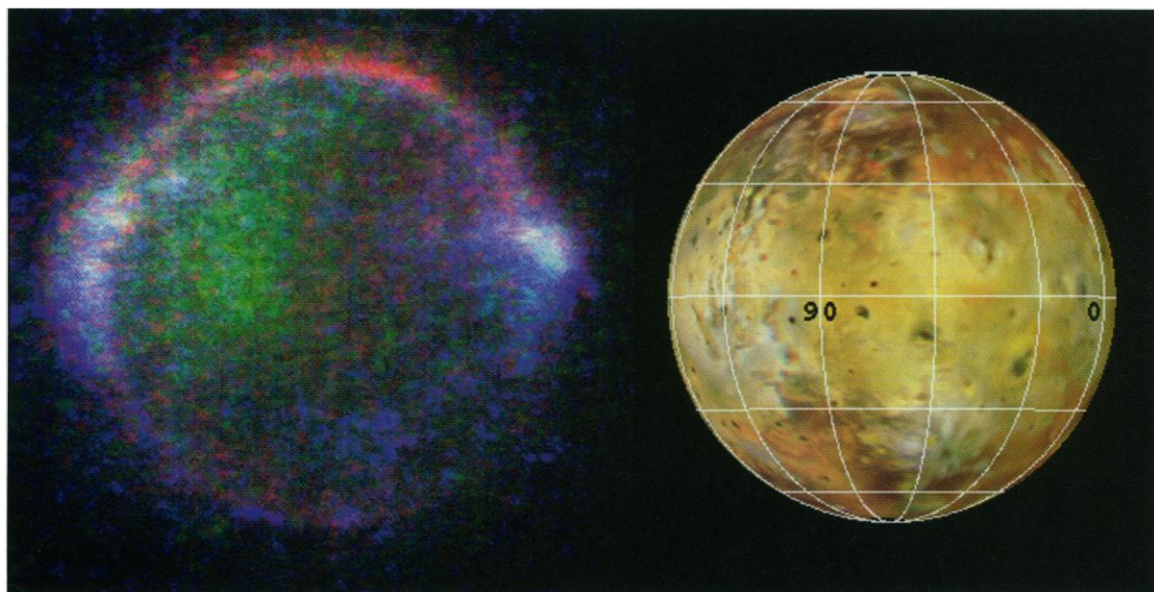
on the surface and did not appear to change position as a function of the geometry of Jupiter's magnetosphere (Fig. 2B). In contrast to the UV equatorial emissions (4), the brighter visible equatorial glows were closely associated with known centers of volcanic activity on Io's surface, including Acala, Kanehekili, and Ra on the sub-Jupiter hemisphere and Prometheus, Culann, Zamama, and Amirani on the anti-Jupiter side. In many of the other eclipse observations, the equatorial glows fluctuated in latitude, in most cases correlated with the positions of the tangent points of the jovian magnetic field lines. SSI images from the earliest orbit (G1) showed differences on the

sub-Jupiter hemisphere, because the Kanehekili and Acala plumes were inactive and the Ra plume was active (18).

To test the association of the blue equatorial glows with specific volcanic plumes, we simulated the appearance of Io in orbit E15, using a three-dimensional plume model with simple ballistic particle trajectories (1, 20). Test particles were launched from fixed surface locations corresponding to known plumes and hot spots, with randomly chosen initial speeds (constrained to be within a fixed range) and launch directions (constrained to lie within 45° of vertical). The trajectories were computed at 100-s intervals, and the positions of the particles at

each time step were recorded for graphical rendering. The best match to the E15 eclipse observations (Fig. 3) was obtained with initial launch speeds between 500 and 1100 m s^{-1}, from the following plumes: Acala (11°N, 334°W), Culann (20°S, 160°W), Prometheus (2°S, 153°W), Zamama (18°N, 173°W), and Amirani (22°N, 114°W). The simulation adequately resembles the observations (compare Fig. 1) but fails to reproduce faint emissions from a cluster of small bright spots west of Acala.

The exact mechanisms that produce Io's colorful glows are not known. Electrons from several sources are available to excite the emissions. Field-aligned Birkeland currents, generated by the motion of the jovian magnetic field past Io, connect Jupiter to Io at the sub- and anti-Jupiter points near the sites of the equatorial plume glows (21). Concentrations of plasma torus electrons are also expected near the sub- and anti-Jupiter points as the plasma flows
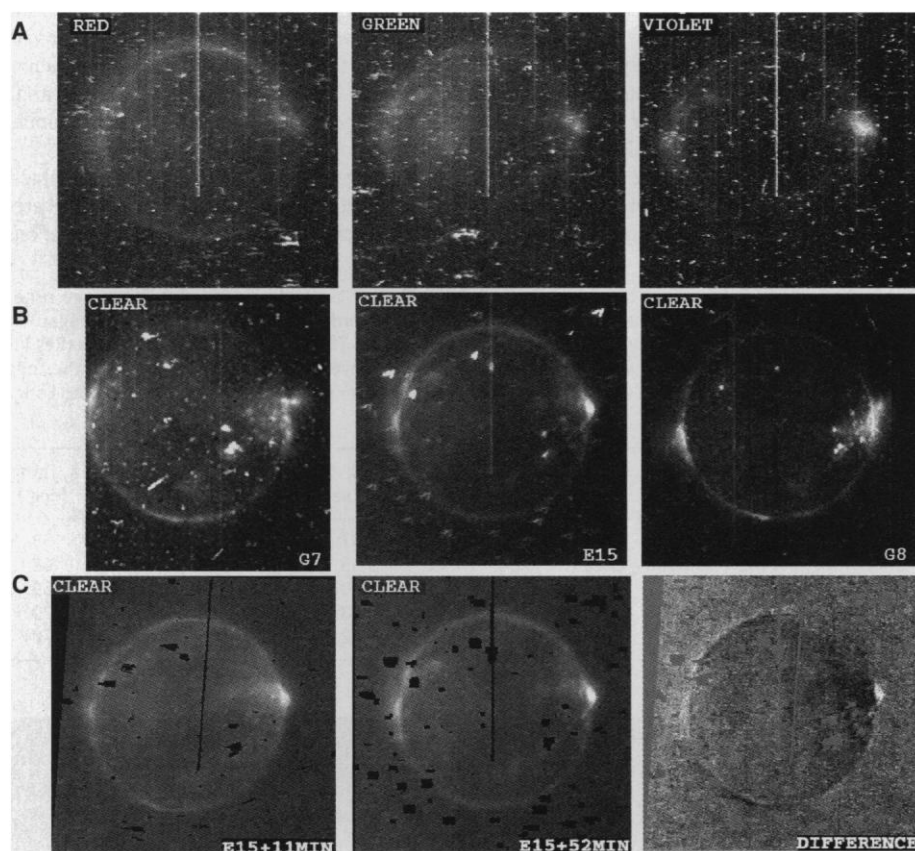

Fig. 2 (top). Raw SSI images of Io in eclipse. (A) Different diffuse emission morphologies can be seen in each of the separate E15 color frames. Two particularly bright volcanoes are visible as spots in the top left of the red-filter frame. (B) A comparison between the E15 clear-filter image (middle) and previous clear-filter pictures taken from slightly different perspectives during orbits G7 and G8. The brightest glow on the sub-Jupiter hemisphere is associated with a volcanic plume (Acala) at a fixed geographic location on the surface and does not appear to change position as a function of the geometry of Jupiter's magnetosphere. (C) Changes in the appearance of Io between 11 min after the start of eclipse (left) and 41 min later (middle). The difference between the two images (right) shows that Io's disk darkened as the eclipse progressed, while the plumes brightened. **Fig. 3 (bottom).** Plume model. Three-dimensional numerical simulation of ballistic trajectories from known volcanic sources on Io's surface. The size of a plume is controlled by the initial launch speeds of the particles (here, between 500 and 1100 m s^{-1}). At least five separate plumes are needed to account for the blue emissions seen in Fig. 1.

Table 2. Brightness and radiated power estimates of Io glows. These estimates are based on the average SSI system response to white light over the bandpasses of each filter, and they may underestimate line emission strengths because of the variation of the filter sensitivity with wavelength. Calculations assume emission at the following wavelengths: violet, 404 nm; green, 560 nm; red, 630 nm; and clear, 560 nm. Measurement uncertainty (standard deviation of the mean) is 25 to 50%. The detection limit in the SSI clear filter is estimated at 2 kR.

Observation	Brightness (nW cm^{-2} sr^{-1})	Brightness (kR)	Power (MW)
Io disk average			
CLR1	1.57	55.4	2414
CLR2	1.21	39.7	1637
VIO	0.32	8.2	472
GRN	0.23	8.0	335
RED	0.17	6.8	254
Acala maximum			
CLR1	8.63	305.2	61
CLR2	11.81	417.7	57
VIO	3.36	85.7	62
GRN	0.84	29.7	8
RED	0.46	18.4	12
Prometheus maximum			
CLR1	5.05	178.6	99
CLR2	7.10	251.3	92
VIO	1.67	42.6	67
GRN	0.54	19.0	27
RED	0.41	16.1	22
North polar limb			
CLR1	2.77	98.1	119
CLR2	2.51	88.7	72
VIO	0.70	17.9	13
GRN	0.48	17.1	20
RED	0.53	21.0	31
Night-side disk			
CLR1	2.17	77.0	798
CLR2	1.54	54.6	597
VIO	0.34	8.7	81
GRN	0.55	19.5	164
RED	0.23	9.2	97

past Io (22). Plasma torus electrons are implicated by the red limb glows, which vary in brightness with the location of the plasma torus center. Photoelectrons from solar UV radiation might also contribute to the excitation of atmospheric emissions on Io, adding to the intensity of the disk glow early in eclipse. More likely, the post-ingress dimming of Io could indicate the partial collapse of an extended sublimation atmosphere superimposed on the presence of localized volcanic gases. The equatorial plume glows, in contrast, actually brighten with time as eclipses progress. Perhaps, as the atmospheric conductivity decreases during eclipse, a greater share of the current through Io is conducted by the volcanic plumes (23).

A major question is the identity of emitting species, which cannot be determined from the broadband SSI observations alone. Many of Io's atmospheric constituents have emission lines at visible wavelengths. Candidate atomic species for the red glow include the forbidden neutral O [O I] lines at 630 and 636 nm, H-α lines at 656 nm, and singly ionized S (S II) lines at 672 and 673 nm. Possible sources for the green glow are [O I] lines at 558 nm and Na I lines at 589 and 590 nm. Recent spectral observations of Io in eclipse from the Keck telescope (9) identified O lines at 630, 636, and 558 nm and found Na D lines at 589 and 590 nm to be brighter than the O green line. Atomic O and Na are thus considered to be the most likely candidates for the red and green glows, respectively. No identifiable emission lines (such as those from O I or O II) were seen from 420 to 445 nm, the portion of the SSI violet-filter bandpass covered by the ground-based observations.

Io's bright blue glows are probably due to molecular emission from SO_2, known to be abundant in volcanic plumes (1, 24). Laboratory spectra of UV-visible emission from SO_2 bombarded by electrons at various energies (6, 25) show molecular bands extending to visible wavelengths that are brighter in violet than in green wavelengths, just as seen in the SSI data. If SO_2 is the source of the blue glows, then Io's spectrum may allow us to constrain the temperature of the electrons exciting the emissions. The threshold energy for exciting the SO_2 (electron states of A − X and one-electron orbitals of a − X) molecular transitions responsible for the UV emission and its visible tail is ~4 eV (6). Sulfur dioxide begins to dissociate at electron energies of 5.6 eV and, for energies greater than ~10 eV, produces a bright spectral feature due to SO that can be seen in the laboratory at 256 nm (6, 25). The nondetection of 256-nm SO emission on Io by HST (17) seems to imply that the blue glows are excited by electrons with energies in the range of 4 to 10 eV. This range includes the mean electron temperature (~5 eV) inferred for the background plasma torus (26). However, these observations were made

at different times (6 years apart), and the electron temperature may vary considerably with time.

If these emissions are due to electron impact excitation, we can estimate the electron densities and column abundances of the emitting species needed to produce the observed brightnesses (27). For electron impact excitation of atomic Na to match the maximum observed night-side disk brightness of 19.5 kR in the green filter, the electron density must be at least an order of magnitude larger than the nominal plasma torus density of 2000 electrons cm^{-3} (28), even if an optically thick column of Na (~10^{13} cm^{-2}) is assumed. Enhanced electron densities of ~20,000 to 40,000 cm^{-3} in the Io plasma wake (29), centered on the leading hemisphere at 90°, may thus be responsible for the broad green night-side emissions. Enhanced electron densities have also been suggested for the "ribbon" in the plasma torus (30). The brighter green emissions on Io's leading night side (Fig. 1, left) could be due to the electron shielding of Na by SO_2 in the thicker leading day-side atmosphere (longitudes of 268° to 88°W) (Fig. 1, right), consistent with the diurnal behavior predicted from atmospheric models (31). Such intense electron impact excitation of atomic O would produce the disk-averaged brightness of 6.8 kR and the maximum brightness at the north polar limb of 21 kR seen in the red filter for column densities of ~1 × 10^{14} cm^{-2} and >1 × 10^{14} cm^{-2}, respectively. This is near the maximum emission brightness of atomic O (at 630 and 636 nm) because it is limited by collisional quenching. Because of attenuation in Io's atmosphere, the population of magnetospheric electrons available at low altitudes to excite the more energetic SO_2 emissions (photons of ~4 to 5.6 eV) is substantially smaller than the population available to excite the less energetic O and Na emissions (~2 eV). If we assume an electron density of 2000 cm^{-3} for the SO_2 glows, then the violet-filter disk-averaged brightness of 8.2 kR and the maximum brightness at Acala of 85.7 kR imply approximate SO_2 column densities of ~10^{16} molecules cm^{-2} and 10^{17} molecules cm^{-2}, respectively. These are more than an order of magnitude larger than the atomic O columns estimated above, similar to model calculations for Io's atmosphere (31).

References and Notes

1. For a comprehensive review, see E. Lellouch, *Icarus* **124**, 1 (1996).
2. Recent observations by the UV spectrometer on Galileo are reported by A. R. Hendrix, C. A. Barth, and C. W. Hord [*J. Geophys. Res.* **104**, 11817 (1999)].
3. R. A. Brown, in *Exploration of the Planetary System, Proceedings of the Symposium, Torun, Poland, September 5–8, 1973*, A. Woszczyk and C. Iwaniszewska, Eds. (Reidel, Dordrecht, Netherlands, 1974), pp. 527–531; L. M. Trafton, *Nature* **258**, 690 (1975); J. T. Trauger *et al.*, *Bull. Am. Astron. Soc.* **8**, 468 (1976); R. A. Brown, *Astrophys. J.* **244**, 1072 (1981); S. T. Durrance, P. D. Feldman, H. A. Weaver, *Astrophys. J. Lett.* **267**, L125 (1983).
4. F. L. Roesler *et al.*, *Science* **283**, 353 (1999).
5. A. F. Cook *et al.*, *ibid.* **211**, 1419 (1981).
6. J. M. Ajello, G. K. James, I. Kanik, *J. Geophys. Res.* **97**, 10501 (1992).
7. J. T. Trauger, K. R. Stapelfeldt, G. E. Ballester, J. T. Clarke, WFPC2 Science Team, *Bull. Am. Astron. Soc.* **29**, 1002 (1997).
8. F. Scherb and W. H. Smyth, *J. Geophys. Res.* **98**, 18729 (1993).
9. M. E. Brown *et al.*, in preparation.
10. M. J. S. Belton *et al.*, *Science* **274**, 377 (1996).
11. A. S. McEwen *et al.*, *ibid.* **281**, 87 (1998).
12. Bandpasses listed are the wavelengths over which the system response to white light is at least 1% of the peak value for each filter, to 5-nm precision [H. Breneman and K. Klaasen, *Report D-5880* (Jet Propulsion Laboratory, Pasadena, CA, 1993)].
13. The E15 color data were recorded with exposure times (25.6 s) longer than those used in previous attempts and were telemetered with lossless compression. An earlier color sequence from orbit G7 was degraded by accidental multiple exposures.
14. K. P. Klaasen *et al.*, *Opt. Eng.* **36**, 3001 (1997). We have subtracted an empirically determined background component, which was calculated as the average brightness of the region surrounding Io's disk. Brightness estimates are based on the average system response to white light over the entire bandpass of each filter. Hence, line emissions may be underestimated if they occur at wavelengths near the limits of the filters' sensitivity.
15. Total optical power is defined as $4\pi JA$, where A is the area of the emission in square centimeters (in the image plane at the distance of the source) and J is the average measured radiance in watts per square centimeter per steradian. Power estimates assume emission at the following wavelengths: violet, 404 nm; green, 560 nm; red, 630 nm; and clear, 560 nm. Depending on the actual spectrum, the sum of the power emitted in the red, green, and violet filters may not necessarily equal that in the clear filter [see also (14)].
16. A. P. Ingersoll *et al.*, *Icarus* **135**, 251 (1998).
17. J. T. Clark, J. Ajello, J. Luhmann, N. Schneider, I. Kanik, *J. Geophys. Res.* **99**, 8387 (1994); G. E. Ballester *et al.*, *Bull. Am. Astron. Soc.* **29**, 980 (1997).
18. A. S. McEwen *et al.*, *Icarus* **135**, 181 (1998).
19. Jupiter is surrounded by a torus-shaped cloud of trapped charged particles that rotate with the planet's magnetic field. The plasma torus is mainly made up of S and O ions and electrons that are continually being replenished by Io. The centrifugal equator of the plasma torus is inclined by ~7° to Jupiter's equatorial plane, so the torus wobbles with respect to Io's position every 13 hours as Jupiter rotates. Io is at maximum north and south magnetic latitudes (that is, farthest from the plasma torus center) for System III magnetic longitudes of ~200° and 20°, respectively, and is in the magnetic equator (the densest part of the plasma torus) at ~110° and 290°, respectively. Embedded within the torus is a narrow vertical band of concentrated plasma known as the "ribbon." The origin of this curious feature is as yet poorly known.
20. See also R. G. Strom and N. M. Schneider, in *Satellites of Jupiter*, D. Morrison, Ed. (Univ. of Arizona Press, Tucson, AZ, 1982), chap. 16. More realistic hydrodynamic simulations [for example, J. V. Austin and D. B. Goldstein, *Bull. Am. Astron. Soc.* **30**, 1121 (1998)] produce plumes that are somewhat flatter than those shown here, owing to shock pressure and horizontal flow.
21. P. Goldreich and D. Lynden-Bell, *Astrophys. J.* **156**, 59 (1969).
22. J. Linker, K. Khurana, M. Kivelson, R. Walker, *J. Geophys. Res.* **103**, 19867 (1998); M. Combi, K. Kabin, T. Gombosi, D. Dezeeuw, K. Powell, *ibid.*, p. 9071; J. Saur, F. M. Neubauer, D. F. Strobel, M. E. Summers, *ibid.*, in press.
23. Possible effects of current flow through Io were described by T. Gold [*Science* **206**, 1071 (1979)] and A. Peratt and A. Dessler [*Astrophys. Space Sci.* **144**, 451 (1988)].
24. J. Pearl *et al.*, *Nature* **280**, 757 (1979); P. Sartoretti *et al.*, *Icarus* **122**, 273 (1996).
25. K. Miller and K. Becker, *Can. J. Phys.* **65**, 530 (1987).

26. E. C. Sittler and D. F. Strobel, *J. Geophys. Res.* **92**, 5741 (1987).
27. For electron impact excitation of Io's atmosphere in eclipse, column abundances were estimated by equating the measured brightnesses to the product of a gas-column density, an average electron density in the gas column, and an average emission rate (for the particular brightness) that depends on the effective electron temperature in the gas column. This linear relation is approximately valid if the gas column is optically thin (not true for Na optical emissions), so that created photons may escape freely without further absorption by the gas column, and if no collisional quenching occurs (not true for O optical emissions at lower altitudes). The determination of the electron temperature and density in the column is a complex problem not addressed here. Instead, we adopt a range of possible values for the electron temperature (to bound the emission rate) of 40,000 K (3.4 eV) to 60,000 K (5.2 eV) and adopt nominal plasma wake values for the electron densi-

ties of 20,000 cm^{-3} for Na and O; we also correct for the brightness for the optically thick Na column. On the basis of these temperatures, the emission rates assumed for Na were 5.4×10^{-7} to 6.8×10^{-7} photons cm^3 s^{-1} [R. Clark, N. Magee Jr., J. Mann, A. Merts, *Astrophys. J.* **254**, 412 (1982)], and the rates for O were 2.4×10^{-9} to 3.2×10^{-9} photons cm^3 s^{-1} (D. Shemansky, private communication). For SO$_2$ located deeper in the atmosphere, an electron temperature of 40,000 K was adopted along with an electron density of 2000 cm^{-3}. An approximate electron impact excitation rate of 1.7×10^{-10} photons cm^3 s^{-1} for the molecular band structures of SO$_2$ appropriate to the SSI violet filter was estimated from laboratory measurements (*6, 25*), with guidance given by K. Becker (private communication).
28. Background plasma torus electron density as measured near Io's orbit in the plasma torus by the Voyager spacecraft is $\sim$2000 cm^{-3} [F. Bagenal, *J. Geophys. Res.* **99**, 11043 (1994)].

29. Electron densities in the Io plasma wake as measured by the Galileo spacecraft are as high as 40,000 cm^{-3}, an order of magnitude larger than the value of $\sim$4000 cm^{-3} measured in the plasma torus near Io [D. A. Gurnett, W. S. Kurth, A. Roux, S. J. Bolton, C. F. Kennel, *Science* **274**, 391 (1996); L. A. Frank *et al.*, *ibid.*, p. 394].
30. M. Volwerk, M. Brown, A. Dessler, B. Sandel, *Geophys. Res. Lett.* **24**, 1147 (1997).
31. M. C. Wong and W. H. Smyth, *Bull. Am. Astron. Soc.* **30**, 1117 (1998); in preparation.
32. We are grateful for informative discussions with many patient colleagues before and during the Madison, Wisconsin, meeting of the Division for Planetary Sciences of the American Astronomical Society. Particular thanks are due to C. Alexander, F. Bagenal, F. Crary, A. Dessler, F. Herbert, W. Hubbard, D. Hunten, K. Klaasen, L. Lane, M. McGrath, K. Rages, and N. Schneider.

Quantitative Assessment of Reactive Surface Area of Phlogopite During Acid Dissolution

Eric Rufe and Michael F. Hochella Jr.

The reactive surface area of a dissolving sheet silicate, phlogopite, was quantitatively assessed in experiments performed in the fluid cell of an atomic force microscope at room temperature and pH values of 2 and 5.7. Additional assessment was provided by surface chemical analysis and electron diffraction. Dissolution rates of phlogopite {hk0} edges are in the range of 10^{-10} moles per square meters per second, two orders of magnitude faster than bulk rates for this mineral. The basal {001} surfaces also show distinct reactivity, although it is short-lived before they become relatively inert. These basal surfaces are shown to leach, hydrate, and expand to an amorphous silica-enriched film.

Chemical weathering of silicate minerals exerts substantial influences on processes such as neutralization of anthropogenic acidic inputs, supplying and cycling of nutrients in natural systems, and long-term climate change by acting as a sink for atmospheric CO$_2$. Laboratory and field-based studies that determine dissolution rates rely on measurements of exposed mineral surface area, but unfortunately, surface area remains one of the most difficult parameters to characterize. Most often, laboratory rates are normalized to the initial surface area measured by a Brunaer-Emmett-Teller (BET) adsorption isotherm. For many silicates, no linear relation exists between rate and BET surface area (*1*), implying that not all of the measured surface area participates in the reaction at the same rate or by the same mechanism. The term "reactive surface area" is often used to distinguish the portions of the surface that dominantly contribute to measured fluxes from portions that

do not. In the literature, the way in which reactive surface area is defined is variable (*2*).

To gain insight into the intricacies of mineral dissolution, others have used in situ atomic force microscopy (AFM) to examine reactions in real time on particular crystallographic faces or microtopographic features of several nonsilicate minerals (*3*). However, there are no published in situ AFM studies in which silicate dissolution rates were measured at room temperature (*4*). Our study combines in situ AFM observations of the dissolution of the mica phlogopite [K$_2$Mg$_6$(Al$_2$Si$_6$O$_{20}$)(OH,F)$_4$] at room temperature with x-ray photoelectron spectroscopy (XPS) and low-energy electron diffraction (LEED) analyses to quantitatively assess reactive surface area (*5*). Among silicates, micas are best suited for investigating the role of reactive surface area because mica dissolution has been well characterized by several solution studies (*6–9*) and because their sheetlike structure allows for the easy identification of surfaces with greatly different reactivity (*10*).

Freshly cleaved phlogopite {001} surfaces were etched in HF to produce crystallographically controlled etch pits (*11*) and then

placed in an AFM fluid cell to which an aqueous solution was introduced (*12*). Dissolution proceeds by the removal of material from the etch pit walls (*13*) (Fig. 1). Etch pits retain the same morphology while dissolving, indicating that each etch pit wall retreats at essentially the same rate. Additionally, no new etch pits nucleate on {001} surfaces. We have imaged the same region of the surface at various times over the course of several days, and the volume of phlogopite removed from a particular etch pit is measured at each time interval (*14*). XPS analysis shows decreasing K/Si, Al/Si, Mg/Si, and F/Si atomic ratios within the first 24 hours of reaction. Because Mg, Al, and K are preferentially removed with respect to Si, the dissolution rates determined from these AFM observations are compared to dissolution rates calculated from Si release reported in solution studies. Dissolution rates were calculated as

$$\text{rate} = \frac{(\Delta V/V_\text{m})}{\text{SA}(t)} \quad (\text{mol m}^{-2}\,\text{s}^{-1}) \qquad (1)$$

where ΔV is the volume of phlogopite removed from the etch pit, V_m is the molar volume of the phlogopite (based on a complete formula unit), t is the time interval, and SA is surface area. Dissolution rates of pit edges measured in this study were normalized to the initial SA of the {hk0} edges (*15*) (Fig. 2). However, dissolution rates of micas in the literature are normalized to the initial BET-measured SA of particles, which includes both {001} and {hk0} surfaces. To compare the rates calculated from an etch pit directly to the rates reported in the literature, it is necessary to construct an imaginary particle with the same edge surface area as that of the etch pit. This was achieved by treating each etch pit as a "negative" particle with the same lateral dimensions as follows. An etch pit Z nanometers deep of size A_initial expands to size A_final during time t. Assume that this is equivalent to a particle Z nanometers thick of size A_final shrinking to size A_initial during time t. The equivalent particle is constructed so that

Department of Geological Sciences, Virginia Polytechnic Institute and State University, Blacksburg, VA 24061–0420, USA.